RSC Applied Interfaces

ROYAL SOCIETY OF CHEMISTRY

PAPER

View Article Online
View Journal | View Issue

Cite this: *RSC Appl. Interfaces*, 2025, **2**, 1259

Nano-cubic $SrTiO_3$ on poly(heptazine imide) (PHI) composite for enhancing photodegradation efficiency†

Phyu Phyu Cho,[a] Phyu Phyu Mon,[a] Mohit Kumar,[ab] Suryakala Duvvuri,[c] Giridhar Madras,[d] Guo-Ping Chang-Chien,[efg] Srinivaas Masimukku[gh] and Subrahmanyam Challapalli *[a]

Received 24th April 2025,
Accepted 14th June 2025

DOI: 10.1039/d5lf00120j

rsc.li/RSCApplInter

Photocatalytic degradation effectively removes organic pollutants from wastewater, ensuring environmental safety. The current study successfully generated $SrTiO_3$ NCs/PHI nanohybrids by a simple sonication method and used them for photocatalytic degradation of organic pollutants. The obtained samples were characterized by XRD, SEM, TEM, XPS, FT-IR, and UV-vis DRS. The results clearly indicated that $SrTiO_3$ nanocubes are effectively spread within the layers of PHI. The catalysts were tested for photocatalytic degradation of crystal violet (CV), methylene blue (MB), rhodamine B (RhB), and Congo red (CR) under UV-visible irradiation. In comparison with other catalysts, $SrTiO_3$ NCs/PHI exhibited exceptional decolorization of all four dyes, and pseudo-first-order kinetics were revealed. The nanocomposite activity exceeded those of $SrTiO_3$ NCs and PHI in increasing charge carrier production, separation, and transport, as validated by PL, EIS, and photocurrent methods. The results of trapping tests showed that $^{\bullet}OH$, $^{\bullet}O_2^-$, and h^+ species are crucial to the degradation process. The type-I heterojunction mechanism was suggested based on the results and Mott–Schottky plots, which were more consistent with the real conditions of the photocatalytic process. This research aims to establish a substantial strategy for enhancing the band structure of $SrTiO_3$ with PHI to improve its photocatalytic efficacy.

1. Introduction

The ongoing progress in science and technology, coupled with rapid industrialization, has made water pollution a major global concern. Industrial wastewater is known to carry a broad spectrum of contaminants, including organic and inorganic pollutants, heavy metals, and other toxic substances.[1] The textile industry utilizes large volumes of water for processes such as dyeing, washing, rinsing, and finishing, resulting in wastewater that poses serious threats to the environment, ecosystems, human health, and overall planetary well-being. The swift expansion of the dye manufacturing sector has heightened concerns over water pollution, shifting attention from dye production itself to the environmental burden caused by wastewater discharge.[2] Often, untreated dye-laden effluents from various industries are released into water bodies, disrupting ecosystems and impacting daily life. Dyes found in industrial wastewater can be classified based on different criteria, such as their chemical structure, origin, and application.[3] For instance, they may be categorized as azo, anthraquinone, phthalocyanine, triphenylmethane, acidic, basic, and reactive dyes by their chemical type, or as natural or synthetic dyes based on their source.

Synthetic dyes, widely produced for numerous industrial applications, include a broad spectrum of types. Based on their structure and ionic nature, they are commonly divided into three main categories: basic, anionic, and cationic dyes.[4] These dyes are extensively utilized across various industries such as textile dyeing, printing, leather processing, paper production, packaging, magnetic toner formulation, and the

[a] *Department of Chemistry, Indian Institute of Technology Hyderabad, Kandi, Sangareddy, 502285, Telangana, India. E-mail: csubbu@iith.ac.in*
[b] *Department of Chemistry and Biochemistry, School of Science Computing and Engineering, Swinburne University of Technology, Hawthorn, VIC, 3122, Australia*
[c] *GITAM (Deemed to be University), Visakhapatnam, Andhra Pradesh, 530045, India*
[d] *Department of Chemical Engineering, Indian Institute of Technology Hyderabad, Kandi, Sangareddy, 502285, Telangana, India*
[e] *Institute of Environmental Toxin and Emerging-Contaminant Research, Cheng Shiu University, Kaohsiung 833301, Taiwan, Republic of China*
[f] *Super Micro Mass Research and Technology Center, Cheng Shiu University, Kaohsiung 833301, Taiwan, Republic of China*
[g] *Center for Environmental Toxin and Emerging-Contaminant Research, Cheng Shiu University, Kaohsiung 833301, Taiwan, Republic of China*
[h] *Conservation and Research Center, Cheng Shiu University, Kaohsiung 833301, Taiwan, Republic of China*

† Electronic supplementary information (ESI) available. See DOI: https://doi.org/10.1039/d5lf00120j

manufacturing of inks and highlighters. Common examples of such dyes include rhodamine B (RhB), methylene blue (MB), Congo red (CR), and crystal violet (CV), which are frequently used in these sectors due to their vivid coloration and functional properties.[5]

Congo red (CR) is an anionic azo dye widely used in textile, paper, and leather industries. It has a complex aromatic structure with sulfonic acid groups, making it water-soluble and resistant to biodegradation. CR is toxic and carcinogenic, and poses serious environmental risks by contaminating water bodies and harming aquatic life. Its persistence and difficulty of removal have led to extensive research on advanced treatment methods for effective degradation and elimination.[6] Crystal violet (CV), methylene blue (MB), and rhodamine B (RhB) are widely used synthetic dyes with toxic and persistent properties. CV is a cationic triphenylmethane dye used in textiles, inks, and microbiology, known for its mutagenic effects.[7] MB, a cationic thiazine dye, is applied in textiles, medicine, and staining, but harms aquatic life and resists degradation.[8] RhB, a cationic xanthene dye, is commonly used in textiles, cosmetics, and fluorescence applications; it is toxic, potentially carcinogenic, and persistent in the environment.[9]

Wastewater treatment involves a range of techniques classified into physical, chemical, biological, and advanced methods.[10] Physical methods, such as sedimentation and filtration, remove suspended solids, while chemical treatments like coagulation, flocculation, and oxidation target dissolved impurities.[11] Biological processes use microorganisms to break down organic matter in systems like activated sludge or anaerobic digesters.[12] Advanced methods, including photocatalysis, adsorption, membrane filtration, and advanced oxidation processes (AOPs), are effective for removing persistent pollutants such as dyes, heavy metals, and pharmaceuticals.[13] An ideal and effective water treatment method should be cost-effective and capable of eliminating toxic species from water, and should not produce harmful residual substances during the treatment process. Photocatalysis is a sustainable and effective approach for dye degradation, offering complete mineralization under mild conditions, low energy input, and potential for real-world wastewater treatment applications. The primary focus among these methods is on photocatalytic processes, particularly semiconductor-based photocatalysts.[14] Photocatalytic dye degradation through solar harvesting remains one of the most promising approaches for water treatment.[15]

Perovskite materials are widely studied for applications in energy storage, sensors, and catalysis due to their unique physical properties.[16] $SrTiO_3$ is considered a viable photocatalyst for water splitting because of its striking physical and chemical characteristics and its suitable conduction band structure.[17] Despite its potential photocatalytic qualities, $SrTiO_3$ has a few drawbacks when it comes to dye photodegradation. Its effectiveness under visible light or sunlight is severely limited by its broad bandgap (~3.2 eV), which limits light absorption to the UV range.[18] Rapid recombination of photogenerated electron–hole pairs is another issue with $SrTiO_3$ that lowers the production of reactive species necessary for dye degradation. Namade *et al.* investigated the photocatalytic activity of $SrTiO_3$ nanoparticles in the degradation of RhB and MB dyes under UV light irradiation.[19] Rezaei *et al.* synthesized a $MoS_2/SrTiO_{3-x}$ photocatalyst *via* a simple two-step hydrothermal method, demonstrating its effectiveness for RhB degradation and the oxygen evolution reaction.[20] Ahmadi prepared a $SrTiO_3$/rGO nanocomposite using a simple method and evaluated its photocatalytic performance for the degradation of rhodamine B (RhB) as a model organic pollutant under UV-vis light.[21] Ganesan synthesized $SrTiO_3$/MWCNT nanocomposites using a simple method, showing enhanced visible light sensitivity and effective MB dye degradation in aqueous solution under visible light.[22]

Performance is further limited by the comparatively small surface area of $SrTiO_3$, which provides few active sites for adsorption and catalytic processes. Long-term stability may be compromised by partial photocorrosion or ion leaching of $SrTiO_3$ in acidic dye solutions. Furthermore, the inadequate valence band alignment and poor charge transport may reduce oxidative power, which reduces the effectiveness of pristine $SrTiO_3$. Overcoming these obstacles requires nanoscale engineering,[23] doping,[24] and the formation of heterojunctions to improve the photocatalytic degradation rate of dyes.[25]

2D carbon-based semiconducting materials are showing great potential based on their light sensitivity and high surface areas, which facilitate the incorporation of nanocatalysts and surface engineering. These materials possess optimal band gaps, the ability to reduce or oxidize water under visible light, the capacity to generate reactive radicals, strong chemical stability, and molecular tunability. Carbon nitrides derived from triazine or heptazine building units are a direct result of high synthesis temperatures, leading to the formation of three different material systems: 1D heptazine-based melon, 2D poly(triazine imide) (PTI), and the recently reported 2D poly(heptazine imide) (PHI).[26] PHI has garnered particular interest due to its remarkable dual properties of light absorption and photogenerated electron storage in the same material. Compared to conventional thermally polymerized graphitic carbon nitride (GCN), which is made from strands of melon units with NH/NH_2 groups and is considered low or semi-crystalline, highly crystalline GCN materials with PHI and PTI structures are emerging as potential high-performance photocatalysts due to their enhanced charge carrier transfer mobility.[27,28]

Poly(heptazine imide) (PHI) is a recently investigated photocatalyst characterized by a large π-conjugation system, well-defined band gap structures (E_g = 2.70 eV), exceptional stability, and abundant surface-active sites, which arise from conjugation condensation in molten salts. Moreover, the anisotropically dispersed CN ring within the PHI structure can significantly enhance charge delocalization, separation, and transmission, in contrast to the low-crystallinity and incomplete-aggregation melon organized in a zigzag

configuration.[29] Thermal solid-state reactions of conventional carbon nitride precursors (cyanamide, melamine) with NaCl, KCl, or CsCl provide an economical and straightforward method for producing poly(heptazine imide) alkali metal salts. The thermodynamic stability of these salts decreases as the size of the metal atom increases. Due to their metastability and excellent structural order, the heptazine imide salts produced exhibit significant activity as photocatalysts in the degradation of rhodamine B and 4-chlorophenol, as well as in Pt-assisted sacrificial water reduction processes under visible light irradiation.[30] Single-atom photocatalysts with Ni^{2+}, Pt^{2+}, or Ru^{3+} have been developed *via* cation exchange using poly(heptazine imides) (PHI) to enhance the degradation of methyl orange and rhodamine B.[31] Additionally, potassium poly(heptazine imide) (PHIK)/Ti-based MOF (MIL-125-NH_2) composites have revealed improved rhodamine B degradation under blue light irradiation.[32] Composites consisting of hydrogen titanate cores with melon and graphitic carbon nitride (g-C_3N_4) shells as sensitizers exhibit significantly better performance in simulated solar (visible) light-driven photodegradation.[33] PHI shows promise for dye photodegradation, but its performance is limited by rapid charge recombination, low surface area, and potential instability under harsh conditions. Enhancements like heterojunction formation or co-catalyst integration are needed to overcome these challenges.

Although various PHI-based composites have shown potential in photocatalysis, the combination of PHI for efficient charge separation with $SrTiO_3$ for strong oxidation ability presents a promising and largely unexplored approach for enhancing photocatalytic performance. The previous study has not reported on the synthesis, characterization, and photoelectrochemical properties of the $SrTiO_3$/PHI photocatalyst. The novelty of this work lies in fabricating a composite catalyst by forming a heterojunction between $SrTiO_3$ and the visible light active polymeric semiconductor poly(heptazine imide) (PHI), aiming to modify the bandgap of $SrTiO_3$ and enhance the degradation of synthetic dyes.

This study aims at synthesizing $SrTiO_3$ nanocrystals (NCs), PHI, and the $SrTiO_3$ NCs/PHI composite through a combination of solid-state and low temperature polycondensation methods. The influence of poly(heptazine imide) (PHI) on the structural, morphological, optical, and electrochemical properties of pure $SrTiO_3$ NCs is investigated, along with its photocatalytic efficiency and recyclability. The mechanisms by which these photocatalysts degrade cationic dyes (CV, MB, RhB) and an anionic dye (CR) under visible light are examined using electrochemical analyses and scavenger trapping tests. The proposed mechanism explains the enhanced photocatalytic activity of the composite, highlighting its potential for efficient organic pollutant degradation. The findings provide a foundation for future research on advanced photocatalysts aimed at enhancing solar-driven pollutant degradation. The $SrTiO_3$/PHI composite shows promising potential for practical applications in wastewater treatment, textile dye removal, and eco-friendly water purification technologies.

2. Experimental section

2.1. Preparation of $SrTiO_3$ nanocrystals

For the preparation of the nanocrystals, 1.476 g of $SrCO_3$ and 0.79 g of TiO_2 were mixed and ground with 22 g of NaCl and KCl mixed powder (with a molar ratio of 50 : 50) in an agate mortar. The mixture was then transferred to a crucible and heated at a ramping rate of 5 °C min^{-1} to 850 °C in a muffle furnace for 6 h. After natural cooling to room temperature, the products were washed with hot water several times. The resulting products were collected by centrifugation, followed by drying at 80 °C overnight, yielding the final products. Subsequently, 1.0 g of $SrTiO_3$ was mixed and ground with 0.25 g of $NaBH_4$ for 20 min in a mortar. The mixture was then heated at a ramping rate of 5 °C min^{-1} to 350 °C for 60 min in an N_2 atmosphere within a tubular furnace. The products were subsequently washed with hot water and ethanol several times and dried at 80 °C.[34]

2.2. Preparation of poly(heptazine imide) (PHI)

Melon was prepared by thermal condensation of melamine and urea. In detail, 1 g of melamine and 10 g of urea were heated to 550 °C for 4 h at a rate of 5 °C min^{-1} in air. The resulting yellow product was ground into powder for further use and denoted as melon.

1 g of melon was ground with KCl (5.1 g), NaCl (5.1 g) and LiCl (4.8 g). The mixture was then heated to 550 °C at a rate of 5 °C min^{-1} for 4 h in a tube furnace under a N_2 atmosphere. The mixture was cooled to 25 °C by natural cooling and the product was then washed with deionized water and dried in an oven at 60 °C.[35]

2.3. Preparation of $SrTiO_3$–poly(heptazine imide) ($SrTiO_3$ NCs/PHI)

A simple sonication method was used to form a heterojunction between $SrTiO_3$ and PHI. Briefly, the as-synthesized PHI (70 mg) and $SrTiO_3$ NCs (30 mg) were dispersed in 40 mL and 20 mL of ethanol under sonication for 30 min, respectively. Two sample solutions were mixed in a beaker and sonicated for 2 h to facilitate the formation of the homogeneous suspension and stirred at 70 °C until the complete evaporation of the solvent was accomplished. The resulting powder was then calcined at 450 °C for 3 h. The final product of $SrTiO_3$ NCs was combined with PHI. The synthesis scheme of $SrTiO_3$ NCs, PHI and $SrTiO_3$ NCs/PHI is described in Scheme 1.

2.4. Characterization of photocatalysts

The crystal structure and phase of the materials were analyzed using X-ray diffraction (XRD) with a PANalytical Model X'Pert PRO diffractometer, equipped with Cu-Kα radiation (λ = 1.54056 Å). The surface morphology was characterized by field emission

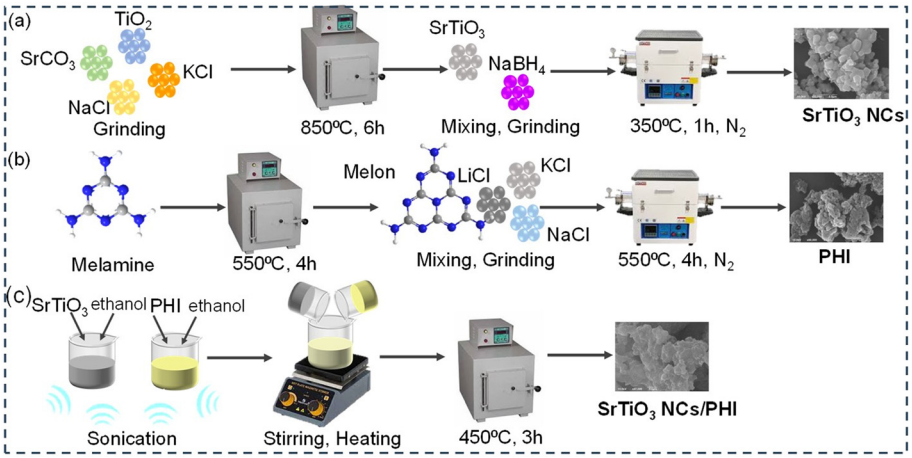

Scheme 1 Schematic representation of the synthesis of (a) $SrTiO_3$ NCs, (b) poly(heptazine imide) (PHI), and (c) the $SrTiO_3$ NCs/PHI composite.

scanning electron microscopy (FESEM; Carl Zeiss, SMTAG). To determine the bandgap energy of the catalysts, $BaSO_4$ was used as a reference in the 200–800 nm wavelength range while recording the UV-diffuse reflectance spectra on a Jasco (V-650) UV-vis spectrophotometer. X-ray photoelectron spectroscopy (XPS) measurements were conducted using an ESCALAB MKIV XPS system to determine the binding energies of the different components in the catalyst. The nitrogen adsorption–desorption isotherms were recorded using a Quantachrome ASIQwin NOVA 2200e Brunauer–Emmett–Teller (BET) surface area analyzer, following degassing of the catalysts at 200 °C under vacuum, to evaluate the surface area and porous nature of the produced catalysts. Photoluminescence spectra were acquired using a Horiba LabRAM HR micro-PL instrument (excitation wavelength: 325 nm; He–Cd laser) to assess the impact of charge separation and electron–hole pair recombination in the catalysts. Electrochemical characterization was performed on a Metrohm AUT302N (Autolab) workstation, which included three electrodes: an indicator electrode, a reference electrode (Ag/AgCl in saturated KCl), and a platinum wire counter electrode.

2.5. Photocatalytic performance

$SrTiO_3$ NCs, PHI, and $SrTiO_3$ NCs/PHI samples were employed as catalysts for the photocatalytic (PC) degradation of four different azo dyes: crystal violet (CV), rhodamine B (RhB), methylene blue (MB), and Congo red (CR), each at a concentration of 10 mg L^{-1}. The photocatalytic experiments were performed by adding 50 mg of the synthesized nanocomposite catalyst to 50 mL of an aqueous dye solution (10 mg L^{-1}) in a glass tube within a reactor, with continuous stirring. The prepared solution was first placed in the dark for 1 h to reach equilibrium. Subsequently, a 500 W tungsten lamp was used to irradiate the dye solution. At predetermined intervals of 30 minutes, 4 mL of the solution was sampled from the reaction tube. The absorption spectra of the extracted samples were recorded in the 200–800 nm range using a UV-vis spectrophotometer. The same procedure was repeated for each catalyst sample, and the photocatalytic degradation efficiency for each dye solution was calculated using the following equation. The degradation efficiency is given by $100 \times (1 - C_t/C_0)$. As the initial concentration is quite low, a first-order equation is obtained and is given by the $-\ln C_t/C_0 = kt$ equation. The concentrations of the dye solution before and after light irradiation are represented by the values C_0 and C_t. The plot of $-\ln C_t/C_0$ *versus* time can be linearly regressed to obtain a straight line, whose slope indicates the apparent first-order rate constant, k.

3. Results and discussion

3.1. XRD analysis

The powder X-ray diffraction (XRD) analysis for $SrTiO_3$ NCs, melon, PHI, and $SrTiO_3$ NCs/PHI is displayed in Fig. 1a. The two primary distinctive peaks observed in melon, located at angles of 13.1° and 27.8°, correspond to the 100 and 002 planes, respectively. These peaks of melon can be attributed to the periodic in-plane structure and interlayer stacking reflection of conjugated aromatic systems. When the periodic arrangements expanded in the plane and the stacking distances between layers decreased, the two major peaks for PHI shifted to 8.1° and 28.3°. Additionally, it is observed that the two primary peaks of PHI exhibit a narrower full width at half-maximum (FWHM) compared to those of melon, indicating a higher degree of crystallinity in PHI. This increased crystallinity is expected to result from the process of molten salt-assisted condensation.[26] No additional peaks were observed for LiCl, KCl, or NaCl in the PHI sample, suggesting the purity of PHI. The diffraction peaks of the $SrTiO_3$ nanocubes exhibited a high degree of sharpness, indicating the strong crystallinity of $SrTiO_3$ NCs. The prominent peaks observed at 2θ angles of 22.9°, 32.4°, 39.9°, 46.4°, 52.3°, 57.9°, 67.8°, 72.6°, and 77.3° correspond to the 100, 110, 111, 200, 210, 211, 220, 221, and 310 planes, respectively (JCPDS No. 73-0661).[36,37] The XRD pattern of the $SrTiO_3$ NCs/PHI composite consisted of peaks corresponding to both $SrTiO_3$ and PHI, indicating the successful formation of the composite.

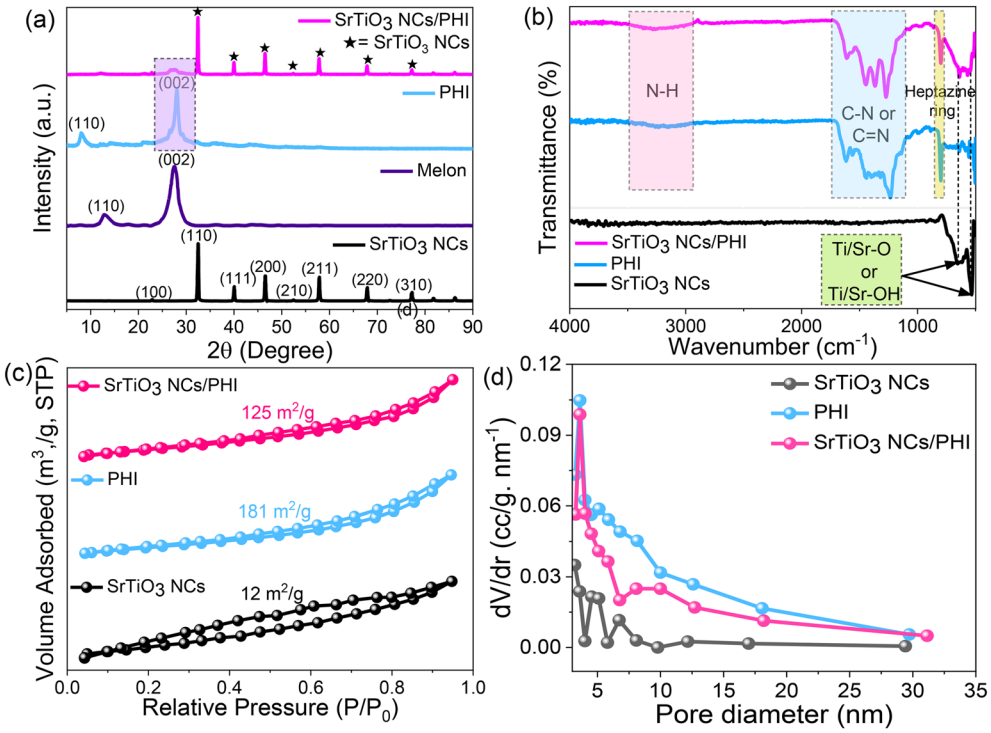

Fig. 1 (a) XRD patterns, (b) FT-IR spectra, (c) adsorption–desorption isotherms, and (d) pore size distribution of pristine $SrTiO_3$, PHI, and $SrTiO_3$/PHI catalysts.

3.2. FT-IR analysis

The $SrTiO_3$ NC sample exhibits two signals at 530 and 650 cm^{-1}, which are associated with Ti–O and/or Ti–OH bonds (Fig. 1b). Additionally, the presence of Sr–O bonds is observed at a wavelength of approximately 837 cm^{-1}.[38] In the PHI material, the signal at 803 cm^{-1} corresponds to the out-of-plane bending mode of the heptazine ring. The prominent peak identified within the 1200–1700 cm^{-1} range can be attributed to the characteristic stretching vibrations of C–N and C═N heterocycles. The broad peak at around 3200 cm^{-1} is attributed to the presence of N–H groups.[39] Therefore, the $SrTiO_3$ NCs/PHI hybrid nanocomposite sample exhibits all the distinctive peaks of both PHI and $SrTiO_3$ NCs. FT-IR analysis confirms the successful fabrication of $SrTiO_3$ NCs/PHI hybrid nanocomposites, which correlates with the XRD analysis.

3.3. Raman analysis

Furthermore, to verify the successful formation of the $SrTiO_3$ NCs/PHI nanocomposites, Raman spectroscopy analysis was carried out. As shown in Fig. S1,† the $SrTiO_3$ NCs exhibit a broad secondary Raman scattering band in the range of 200 to 499 cm^{-1}, indicative of continuous broadband features.[40] The characteristic Raman peaks of $SrTiO_3$ NCs are observed at 293, 565, 761, 823, 984, and 1197 cm^{-1}.[41,42] In addition, two distinct bands appear at 1340 cm^{-1} (D band) and 1520 cm^{-1} (G band) in the $SrTiO_3$ NCs/PHI nanocomposites, corresponding to the disordered and graphitic carbon structures of PHI, respectively.[43] These observations confirm the successful incorporation of $SrTiO_3$ NCs into the PHI matrix. Therefore, the combined PXRD and Raman analyses unequivocally confirm the successful synthesis of the $SrTiO_3$ NCs/PHI nanocomposites.

3.4. BET analysis

To examine the impact of $SrTiO_3$ nanocube addition on the surface characteristics, Brunauer–Emmett–Teller (BET) analysis was conducted to explore the specific surface area and porosity of $SrTiO_3$ NCs, PHI, and $SrTiO_3$ NCs/PHI nanocomposites by measuring the nitrogen adsorption–desorption isotherms. As shown in Fig. 1(c and d), the specific surface areas for the $SrTiO_3$ NCs, PHI, and $SrTiO_3$ NCs/PHI nanocomposites were found to be 12, 181, and 125 $m^2\ g^{-1}$, respectively, while the total pore volumes were in the range of 0.024, 0.335, and 0.244 $cm^3\ g^{-1}$, respectively. Moreover, the average adsorption pore diameters for $SrTiO_3$ NCs, PHI, and $SrTiO_3$ NCs/PHI were found to be 3.18, 3.60, and 3.60 nm, respectively, further confirming the mesoporous nature of the nanocomposites.

3.5. Morphological analysis

The surface morphology and structural properties of $SrTiO_3$ NCs, PHI, and $SrTiO_3$ NCs/PHI nanocomposites were analyzed by HR-SEM and TEM. Fig. 2a exhibits the structure of the $SrTiO_3$ nanocubes. The image demonstrates the $SrTiO_3$ in a cube morphology, with a nearly uniform particle size.[44,45] Additionally, TEM analysis was carried out to further confirm the formation of cubic-shaped $SrTiO_3$ in Fig. 2b with an

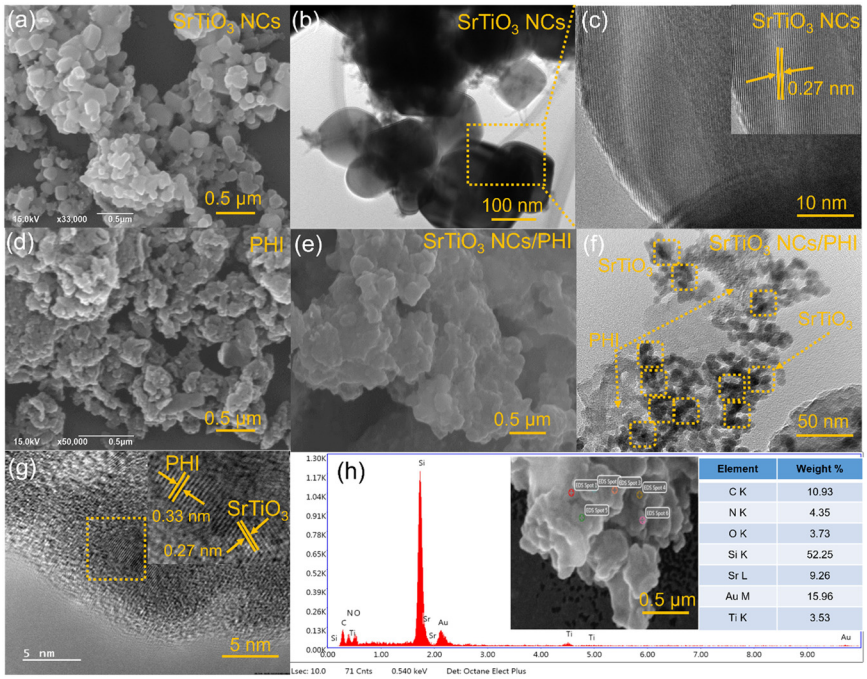

Fig. 2 (a, d and e) SEM images of $SrTiO_3$ NCs, PHI, and $SrTiO_3$ NCs/PHI, (b and f) TEM images of $SrTiO_3$ NCs and $SrTiO_3$ NCs/PHI, (c and g) high-resolution TEM images of $SrTiO_3$ NCs and $SrTiO_3$ NCs/PHI, and (h) EDS spectrum of the $SrTiO_3$ NCs/PHI composite on a silicon wafer.

average diameter of about 100 nm. The high-resolution TEM (HRTEM) image indicated that pure $SrTiO_3$ NCs exhibited high crystalline features with a fringe width of 0.27 nm corresponding to the (110) plane for $SrTiO_3$ NCs (Fig. 2c).[34] Fig. 2d depicts the morphology of PHI; the accumulated layered structure of PHI was observed, owing to the planar graphitic-like structure. In addition to Fig. 2e, the nanocomposites ($SrTiO_3$ NCs/PHI) revealed that the $SrTiO_3$ cubes were dispersed homogeneously on the surface of the PHI. FESEM-EDS validated the presence of $SrTiO_3$ NCs in the $SrTiO_3$/PHI composite (Fig. 2h). As for the combined $SrTiO_3$ and PHI sample ($SrTiO_3$/PHI), the particle size was reduced to ~50 nm with the morphology remaining intact (Fig. 2f). The HRTEM image for $SrTiO_3$ NCs/PHI is presented in Fig. 2g and the lattice plane spacing was determined to be 0.27 nm which is compatible to (110) for $SrTiO_3$ NCs and 0.33 nm which is compatible to (002) for PHI correlating with the XRD analysis. The SEM and TEM images of the $SrTiO_3$/PHI composite revealed a layered structure, where the PHI sheets are uniformly coated with nano-cubic $SrTiO_3$, indicating a favourable morphology for internal charge transfer during photocatalysis. Additionally, energy-dispersive X-ray (EDX) analysis confirmed the presence of all constituent elements, verifying the successful formation of the hybrid composite.

3.6. XPS analysis

XPS analysis was conducted to investigate the surface properties and oxidation states of the elements in the $SrTiO_3$ NCs/PHI catalyst (Fig. 3). The survey spectrum (Fig. 3a) confirms the presence of key elements, including C (1s), N (1s), Sr (3d), Ti (2p), and O (1s), within the $SrTiO_3$ NCs/PHI catalyst. The Sr 3d spectrum exhibits peaks at binding energies of 133.2 eV and 134.2 eV, corresponding to Sr $3d_{5/2}$ and Sr $3d_{3/2}$, respectively (Fig. 3b).[46] The Ti 2p spectrum exhibits a splitting into two distinct peaks with binding energies of 454.6 eV and 460.1 eV, representing the Ti $2p_{3/2}$ and Ti $2p_{1/2}$ doublet states (Fig. 3c). The O 1s peak is resolved into two distinct peaks at 529.8 eV and 532.9 eV, corresponding to different types of oxygen species: lattice oxygen and adsorbed oxygen (Fig. 3d).[47] The deconvolution of the C 1s spectrum reveals three distinct peaks with binding energies of 284.6 eV, 289.4 eV, and 292.2 eV, corresponding to C–C, C=O, and C–N–C bonds, respectively (Fig. 3e).[48,49] The N 1s spectrum displays distinct peaks at 398.1 eV, 399.5 eV and 401.8 eV, indicating various chemical states of nitrogen, including Ti–N, O–Ti–N or Ti–N–O, and N–O, respectively (Fig. 3f).[50] The XPS results indicate that the hybrid composite exhibits characteristic features of both $SrTiO_3$ NCs and PHI, suggesting the formation of a strong interfacial interaction between the two components. This intimate contact is expected to facilitate efficient charge carrier transfer, thereby enhancing the photocatalytic performance. The XPS spectra of pristine $SrTiO_3$ NCs and PHI (Fig. S2 and S3†) demonstrate their respective elemental binding energies.

3.7. Optical properties

The UV-visible optical absorption characteristics of the $SrTiO_3$ NCs, PHI, and $SrTiO_3$ NCs/PHI composite catalysts were determined using UV diffuse reflectance spectra

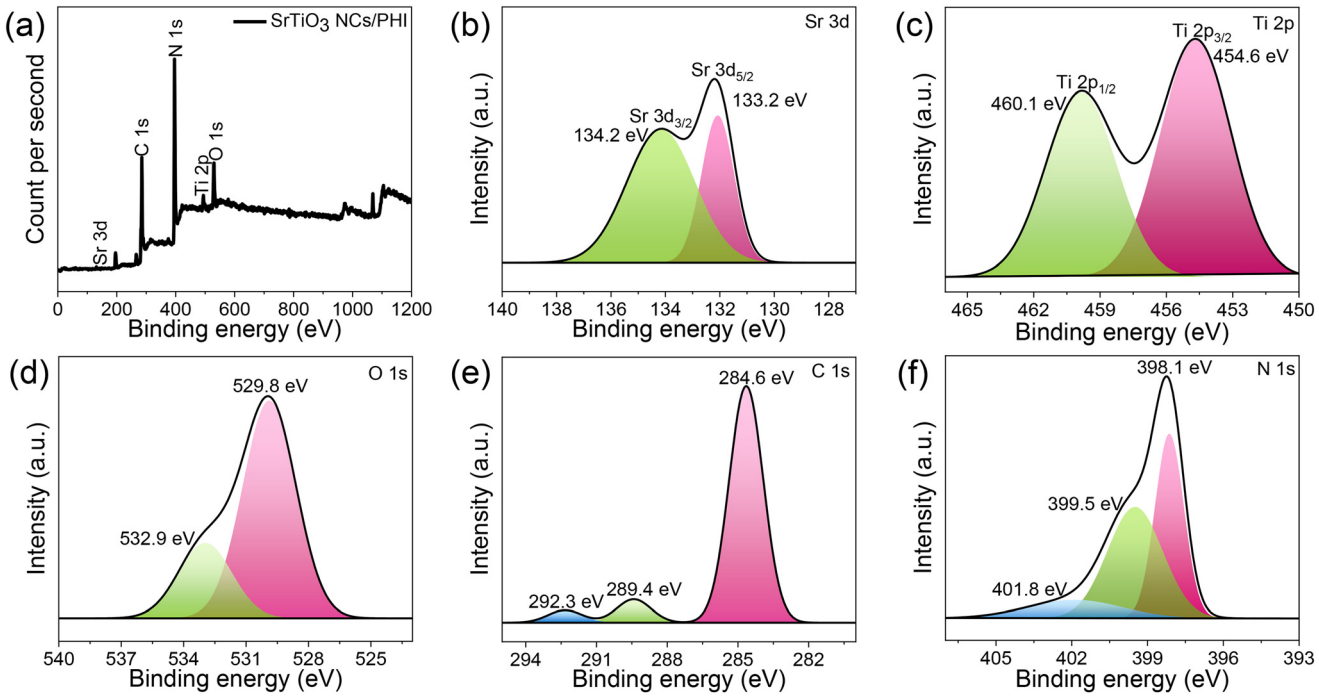

Fig. 3 (a) Survey scan of $SrTiO_3$ NCs/PHI and high resolution XPS spectra of (b) Sr 3d, (c) Ti 2p, (d) O 1s, (e) C 1s, and (f) N 1s.

(Fig. 4a). The catalysts have distinct absorption thresholds, with certain catalysts even falling within the visible spectrum. The bandgap energies of the catalysts were determined by using the modified Tauc, Davis, and Mott equation to the data presented in Fig. 4a.

$$(\alpha h\gamma)^{1/n} = A(h\upsilon - E_g)$$

The absorption coefficient (α) is a function of the reflectance ($F(R)$), and it is influenced by various factors such as Planck's constant (h), vibration frequency (n), bandgap (E_g), proportional constant (A), and the nature of the transition (n). The intercept of the linear part in the plot of photon energy ($h\upsilon$) *vs.* $[F(R)\ h\upsilon]^{1/2}$ directly provided the bandgap energy of the catalysts. The bandgap energy of $SrTiO_3$ NCs is

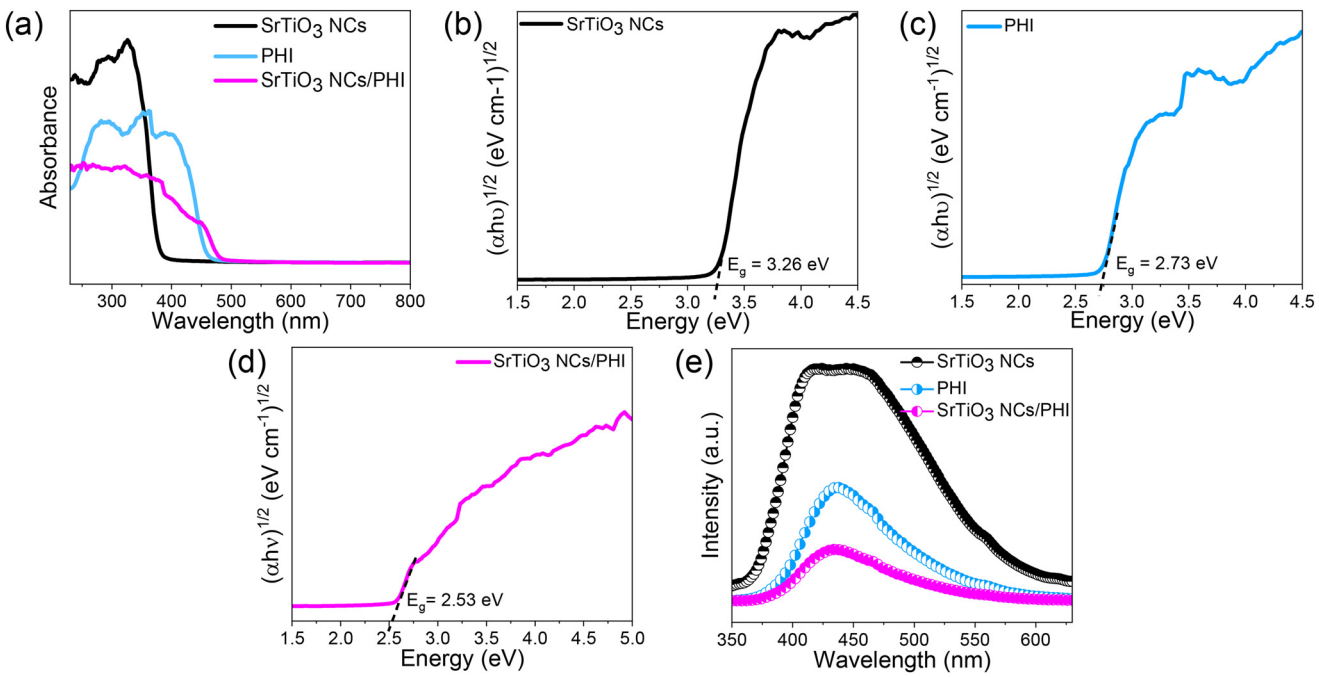

Fig. 4 (a) UV-DRS spectra, (b–d) Tauc plot and (e) PL spectra of $SrTiO_3$ NCs, PHI, and $SrTiO_3$ NCs/PHI catalysts.

the highest, measuring 3.25 eV, whereas PHI has a bandgap of 2.73 eV (Fig. 4b–d). The bandgap measurements indicate that bare $SrTiO_3$ NCs are only active in the ultraviolet (UV) area, while the bare PHI and the $SrTiO_3$ NCs/PHI composite have significant bandgap values of 2.53 eV, indicating activity in the visible light range.

The optical band gap of $SrTiO_3$ in this study was 3.25 eV, as determined by UV-vis diffuse reflectance spectroscopy using a Tauc plot. This value is consistent with previously reported experimental values for bulk $SrTiO_3$, which range from 3.2–3.3 eV.[51–53] Based on electronegativity values and validated through literature comparisons, the conduction band minimum (CBM) and valence band maximum (VBM) were determined to be −0.633 eV and +2.63 eV *vs.* NHE, respectively. $SrTiO_3$ is suitable for UV-driven photocatalytic applications due to the experimentally observed wide band gap and deep valence band. These results are consistent with this. In contrast, the band gap is significantly underestimated by density functional theory (DFT) calculations that employ standard exchange–correlation functionals, such as the local density approximation (LDA) or generalized gradient approximation (GGA), which typically predict values of 1.8–2.1 eV.[54,55] Using hybrid functionals such as HSE06 or GW approximations, which account for electron–hole interactions and produce band gaps in the range of 3.2–3.3 eV, more precise theoretical predictions have been made, closely matching experimental observations. This comparison underscores the necessity of employing sophisticated theoretical methods to precisely characterize the electronic and optical properties of wide-band-gap oxides, such as $SrTiO_3$.[56]

Poly(heptazine imide) (PHI) demonstrated an optical band gap of 2.73 eV in this study, calculated from UV-vis diffuse reflectance data using the Tauc method. The conduction and valence band edges were found to be positioned at −0.533 eV and +2.20 eV *vs.* NHE, respectively. These results align well with reported experimental values, where PHI typically exhibits a band gap in the range of 2.7–2.8 eV, depending on the degree of polymerization, crystallinity, and synthesis approach.[57,58] The negative conduction band edge indicates the potential of PHI for driving hydrogen evolution under visible light. Theoretical studies using conventional DFT methods, such as those employing GGA or LDA functionals, often report underestimated band gaps between 1.8 and 2.2 eV due to their inability to accurately capture electronic exchange and correlation effects.[59,60] In contrast, DFT calculations with hybrid functionals like HSE06 have provided more realistic predictions, with calculated band gaps approaching experimental values and more accurate band edge alignment.[61] These findings confirm that PHI possesses a favourable electronic structure for visible-light photocatalysis and underscore the importance of using advanced theoretical models for precise band structure determination.

Recombination of electron–hole pairs is a significant constraint for semiconductor photocatalysts, as it reduces their photocatalytic activity. Typically, a higher PL intensity corresponds to a higher rate of charge carrier recombination and a lower level of photocatalytic activity. The intensity of PL emission is also dependent upon the radiation and surface structural shortcomings of the photocatalyst, as well as the synthesis situations. In Fig. 4e, $SrTiO_3$ NCs exhibited the highest photoluminescence (PL) intensity, suggesting the most rapid recombination of electron–hole pairs. On the other hand, PHI had relatively low PL intensity, indicating the slowest recombination rate of electron–hole pairs. The photoluminescence (PL) intensity of the $SrTiO_3$ NCs/PHI catalyst was seen to be markedly reduced. These data validate that these catalysts exhibit superior photocatalytic properties compared to the bare catalysts.

3.8. Study of photocatalytic activity on organic dyes

For various kinds of pollutants made up of cationic and anionic organic dyes, the photocatalytic activity of the as-synthesized photocatalysts was examined. The developed photocatalysts were also tested for their universal applicability by using them with various cationic dyes. Fig. 5(a and b) reveal that under the same experimental conditions, the $SrTiO_3$ NCs/PHI heterojunction demonstrated excellent photocatalytic activity toward CV, with 96% degradation in 90 min, while the photocatalytic activities of bare $SrTiO_3$ NCs and PHI were 34% and 90%, respectively. Aside from CR and CV, $SrTiO_3$ NCs presented notable photocatalytic activity toward MB degradation, breaking down 94% of MB in 90 min, whereas only 8% and 59% of MB were broken down by $SrTiO_3$ NCs and PHI, respectively (Fig. S4†). Fig. S3† further demonstrates the high photocatalytic activity of the $SrTiO_3$ NCs/PHI heterojunction toward the RhB dye, with 94% decomposition possible in 150 min, compared to just 7% and 74% for $SrTiO_3$ NCs and PHI, respectively, under comparable conditions. The anionic dye CR was used to test the photocatalytic capabilities of the synthesized photocatalysts. $SrTiO_3$ NCs/PHI demonstrated excellent photocatalytic activity, degrading 85% of CR in 90 min when exposed to solar light. Under the same conditions, only 7% and 75% of CR were degraded by $SrTiO_3$ NCs and PHI, respectively (Fig. 5(c and d)). When compared to the photocatalytic activity of bare PHI and $SrTiO_3$ NCs, the $SrTiO_3$ NCs/PHI heterojunction exhibited superior activity against all pollutants. This was attributed to its extension of the optical absorption zone, large surface area, and effective charge separation. Furthermore, for the photodegradation of various dyes, the photocatalytic performance of the generated $SrTiO_3$ NCs/PHI heterojunction was also compared with those of previously reported photocatalysts (Table 1). This suggests that the synthesized photocatalyst is a viable option for use in organic dye treatment in environmental remediation and has practical applications. For all pollutants studied (CV, RhB, MB, and CR), the heterojunction $SrTiO_3$ NCs/PHI exhibits a higher reaction rate compared to bare PHI and

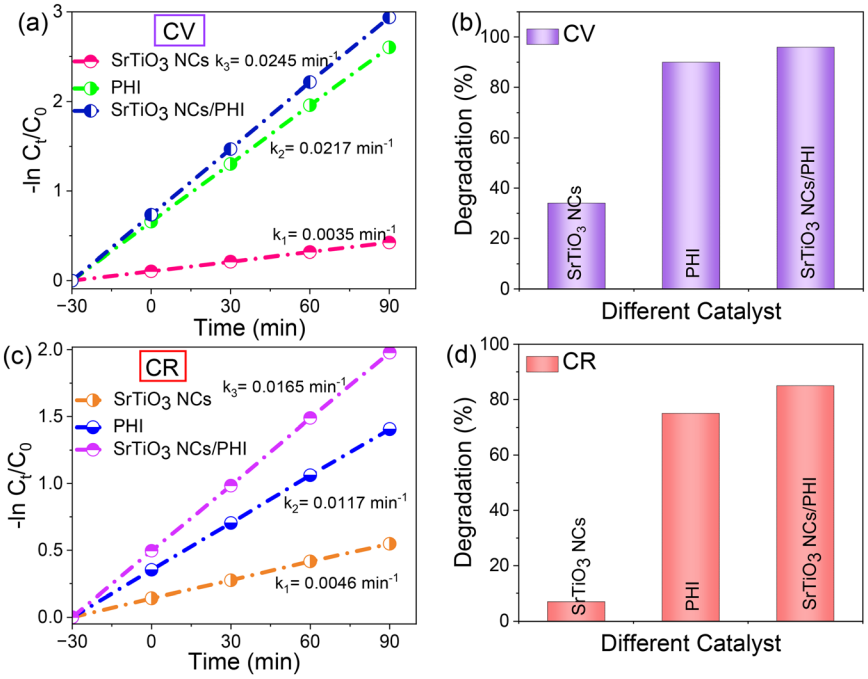

Fig. 5 (a and c) Kinetic rate constant plots and (b and d) photocatalytic degradation efficiency of the as-prepared samples on CV and CR under UV-visible light irradiation. Reaction conditions: concentration and volume of pollutants (CV and CR) = 10 ppm and 50 mL, amount of catalyst = 50 mg.

Table 1 Comparison of the photocatalytic activity of the developed $SrTiO_3$ NCs/PHI heterojunction with those of previously reported $SrTiO_3$ photocatalysts for the photodegradation of different dyes

Sr No.	Photocatalyst	Pollutant	Time (min)	Light source	Degradation efficiency (%)	Ref.
1	Al–$SrTiO_3$	CR	90	UV	81	34
2	N–$SrTiO_3$	MO	240	UV	95	42
3	g-C_3N_4/$SrTiO_3$:N@$ZnFe_2O_4$	RhB	30	Visible	90	62
4	Ag@$SrTiO_3$@CNT	MO, RhB, MB	90	Visible	46, 71, 100	63
5	$SrTiO_3$/g-C_3N_4	MB	420	Visible	40	64
6	**$SrTiO_3$·NCs/PHI**	CV, RhB, MB, and CR	90, 150, 90 and 90	UV-visible	96, 94, 94 and 85	This work

$SrTiO_3$ NCs. Specifically, under identical experimental conditions, the kinetic rate constant of the heterojunction for dye photodegradation is faster than those of bare $SrTiO_3$ NCs and PHI. The enhanced reaction rate of the $SrTiO_3$ NCs/PHI heterojunction can be attributed to its larger surface area, extended full-spectrum light absorption, band gap narrowing, and efficient charge transfer of photogenerated charge carriers.

The mineralization property of the $SrTiO_3$·NCs/PHI heterojunction on CV, RhB, MB, and CR pollutants during UV-visible light irradiation was evaluated by examining the total organic carbon (TOC). The TOC of CV, RhB, MB, and CR before and after photocatalysis by the $SrTiO_3$ NCs/PHI heterojunction is displayed in Fig. S5.† After photocatalysis, the TOC decreased by 75%, 87%, 86% and 90% indicating that CR, CV, MB, and RhB mineralized into CO_2 and H_2O.

3.8.1. Photocatalytic activity under different reaction conditions. The various conditions of operation have a significant impact on the way a catalytic system performs. The effects of the initial pollutant concentration, catalyst dosage, solution pH, and different scavengers on CV and CR photodegradation were examined to optimise $SrTiO_3$ NCs/PHI.

Effect of concentration on photocatalytic properties. The photodegradation efficiency decreases with increasing pollutant concentration for CV and CR (Fig. 6a and 7a). The impact of pollutant concentration on the catalytic capacity for photocatalysis was further evaluated. The existence of more pollutant molecules than accessible active sites on the photocatalyst may be the cause of the decrease in photodegradation efficiency of the catalyst with an increase in pollutant concentration. Additionally, the presence of more dye molecules at greater dye concentrations may result in less light reaching the photocatalyst surface, which would reduce the catalytic activity even more.[65] The dye concentration of 10 ppm was chosen for additional research since it showed the highest photodegradation efficiency.

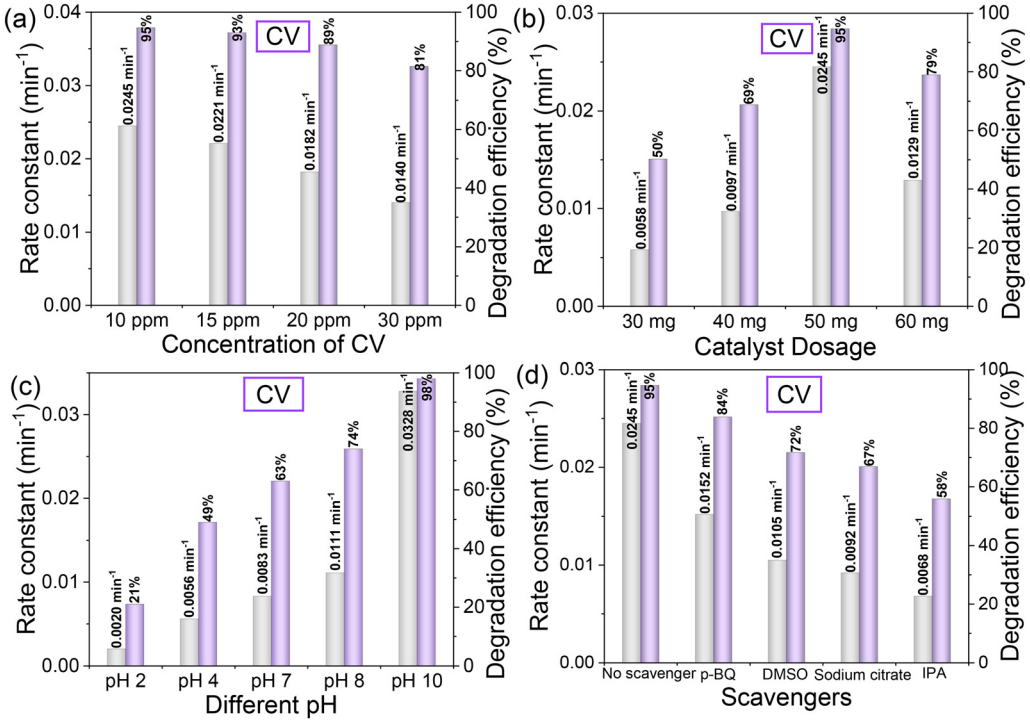

Fig. 6 Photocatalytic degradation efficiency and kinetic rate constant of the as-prepared sample ($SrTiO_3$ NCs/PHI) for (a) the effect of concentration (CV), (b) catalyst dosage, (c) effect of pH, and (d) scavenging tests under UV-visible light irradiation.

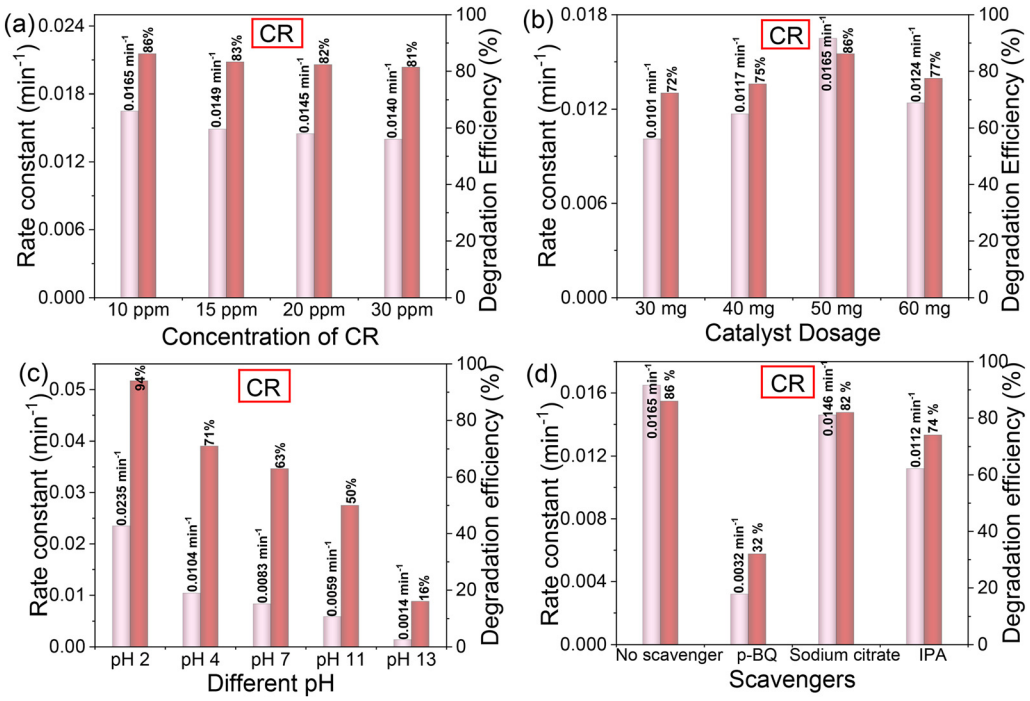

Fig. 7 Photocatalytic degradation efficiency and kinetic rate constant of the as-prepared sample ($SrTiO_3$ NCs/PHI) for (a) the effect of concentration (CR), (b) catalyst dosage, (c) effect of pH, and (d) scavenging tests under UV-visible light irradiation.

Effect of catalyst dosage on photocatalytic performance. Catalyst dosage was examined by increasing from 30 to 40, 50, and 60 mg while maintaining constant values for other parameters to investigate whether it affected CV and CR photodegradation. As the catalyst dosage increased from 30 to 50 mg of $SrTiO_3$ NCs/PHI, Fig. 6b and 7b demonstrate that

the photodegradation efficiency of CR and CV dramatically improved to 86% and 95% within 90 min. Nevertheless, the efficiency of photodegradation decreases with additional increases in photocatalyst dosage. The higher catalyst dosages have a negative effect because of aggregation, photon scattering, suspension turbidity, and masking of the photosensitive surface. As a result, the photocatalytic activity is reduced when photon penetration into the solid phase is hindered.[66,67]

Effect of pH on the photocatalytic performance. Fig. 6c and 7c demonstrate an investigation into the effects of pH on the photocatalytic performance of the $SrTiO_3$ NCs/PHI heterojunction in CV and CR degradation. The photocatalytic performance of the catalyst is significantly impacted by pH. The influence of pH on CV photodegradation was investigated; Fig. 6c indicates that pH 10 is the optimal pH for CV photodegradation, which can process 98% of the compound. At pH 2, CR exhibited the highest photodegradation efficiency (94%) of any catalyst. The pseudo-first order kinetic rates of the parameters (concentration effect, dosage effect, pH effect) of the photodegradation of CV and CR are described in Fig. 6c and 7c. $-\ln C_t/C_0$ *vs.* time plots for photocatalytic parameters are illustrated in Fig. S6 and S7.†

3.9. Photoelectrochemical properties of $SrTiO_3$ NCs, PHI and the $SrTiO_3$ NCs/PHI composite

Photoelectrochemical measurements were performed in a 3-electrode setup 0.3 M Na_2S + 0.35 M Na_2SO_3 (pH 12.5) with Pt as the counter electrode and Ag/AgCl (3 M KCl) as the reference electrode. As described in Fig. 8a, the photocurrent density *vs.* potential (*J*–*V*) curves were obtained under continuous illumination of AM 1.5G. $SrTiO_3$ NCs delivered a photocurrent

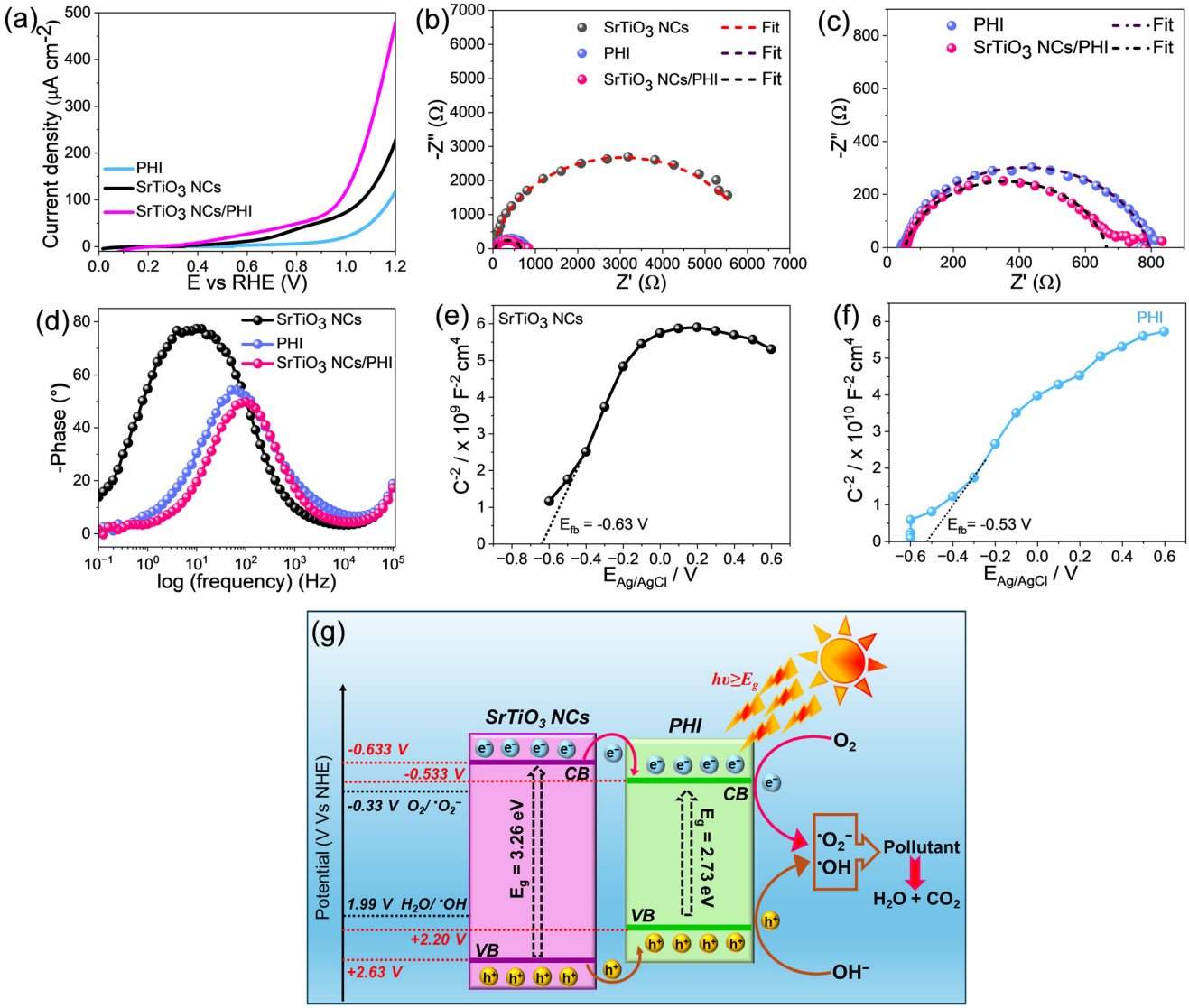

Fig. 8 (a) Polarization curves, (b and c) electrochemical impedance spectra, (d) Bode phase plots of $SrTiO_3$ NCs, PHI, and $SrTiO_3$ NCs/PHI photoelectrodes, Mott–Schottky (M–S) plots of (e and f) $SrTiO_3$ NCs and PHI, and (g) possible reaction mechanism for multi-dye degradation.

Table 2 Electrochemical impedance data fitting parameters of the photoelectrodes

	R_s (Ω)	R_{ct} (Ω)	CPE (F)
PHI	58	6095	$4.89 \times 10^{-0.5}$
$SrTiO_3$ NCs	45	794	$1.56 \times 10^{-0.5}$
$SrTiO_3$ NCs/PHI	53	663	$1.07 \times 10^{-0.5}$

of 230 μA cm^{-2} at 1.2 V_{RHE}, while PHI exhibited much less PEC activity (130 μA cm^{-2} at 1.2 V_{RHE}). However, the composite of $SrTiO_3$ NCs and PHI showed an ameliorated photocurrent density (470 μA cm^{-2} at 1.2 V_{RHE}), which is 2-fold photoactivity as compared to that of $SrTiO_3$ NCs and nearly 4-fold that of PHI (Fig. 8a and S8†). To gain insight into charge transfer and the mechanism, electrochemical impedance spectroscopy (EIS) revealed that the heterojunction of $SrTiO_3$ NCs/PHI showed the lowest charge transfer resistance (R_{ct} = 663 Ω) and faster charge transfer kinetics as compared to $SrTiO_3$ NCs (R_{ct} = 794 Ω) and PHI (R_{ct} = 6095 Ω), respectively (Fig. 8(b and c)). The heterojunction facilitated the quick movement of charge and better separation of electron–hole pairs upon photoexcitation. The fitted parameters are presented in Table 2, which clearly demonstrates the improved properties of $SrTiO_3$ NCs, PHI and $SrTiO_3$ NCs/PHI upon exposure to light. The Bode phase plot was obtained to gain insight into the electron lifetime in the circuit. The plot of phase difference (degree) *vs.* frequency (Hz) revealed the lowest time for $SrTiO_3$ NCs/PHI, whereas PHI showed the highest time period insinuating that the kinetics of charge transfer is fastest in $SrTiO_3$ NCs/PHI and slowest in PHI owing to the formation of the heterojunction and the internal electric field formed at the $SrTiO_3$ NC and PHI heterojunction (Fig. 8d).

3.10. Recyclability and stability

The recyclability and stability of the $SrTiO_3$ NCs/PHI catalyst were evaluated through multiple cycles of degradation, with the results (XRD and XPS) presented in Fig. S9.† The slight decrease in photoactivity observed after each successive cycle can likely be attributed to catalyst loss during the washing and drying processes, as well as the presence of a small amount of degradation products on the catalyst's surface. However, after regeneration by heating at 80 °C for 12 hours, the photodegradation efficiency of the catalyst is nearly identical to that of the fresh sample, demonstrating the reusability of this composite catalyst. To evaluate the environmental applicability and sustainability of the $SrTiO_3$/PHI photocatalyst, recyclability and structural stability tests were conducted. The composite retained high photocatalytic performance over five consecutive degradation cycles, demonstrating excellent reusability. Furthermore, post-reaction XRD and XPS analyses confirmed the preservation of the crystal structure and surface chemical states, indicating strong structural and chemical stability under photocatalytic conditions. These results suggest that the $SrTiO_3$/PHI hybrid photocatalyst is not only effective but also robust and potentially suitable for long-term use in practical environmental remediation.

X-ray photoelectron spectroscopy (XPS) was used to compare the surface elemental composition before and after reuse to assess the stability of the produced $SrTiO_3$ NCs/PHI catalyst during photocatalytic degradation. Potential ion leaching is indicated by the atomic and mass percentages of titanium (Ti) and strontium (Sr). The atomic percentages of Sr and Ti in the fresh $SrTiO_3$ sample were determined to be 1.5% and 0.8%, respectively, with corresponding mass percentages of 2.8% for Ti and 8.8% for Sr. These values dramatically plummeted following the catalyst's photocatalytic degradation and reuse: Sr fell to 0.2% (atomic) and 1.4% (mass), while Ti fell to 0.5% (atomic) and 1.9% (mass) (Table S1†). Ion leaching, in which Sr^{2+} and Ti^{4+} ions are liberated from the $SrTiO_3$ surface into the reaction medium during the photocatalytic process, is evident from this significant decrease in both atomic and mass percentages.[68,69] The more noticeable drop in Sr concentration indicates that Sr ions are more prone to leaching, most likely because of their surface exposure and dynamic interaction with photogenerated holes or reactive oxygen species when exposed to light. Such ion leaching suggests possible structural integrity degradation over several cycles in addition to confirming partial photocorrosion of the catalyst surface.[70] These results demonstrate that to prevent leaching and improve the longevity of the $SrTiO_3$ NCs/PHI photocatalyst, surface stabilizing techniques like protective coatings or dopant incorporation are essential. Previously Havlik *et al.* found out a similar pattern in their report.[71]

3.11. Analysis of CV and CR degradation intermediates by LC/MS

The identification of intermediate products during the degradation of organic pollutants is crucial, as these intermediates can often exhibit greater toxicity than the original compound. The LC-MS spectra shown in Fig. S10† illustrate the degradation pathway of crystal violet (CV). In Fig. S10a,† the strong molecular ion peak at *m*/*z* 372.24 corresponds to the intact CV molecule.[72–74] After photocatalytic treatment, Fig. S10b† reveals several new peaks at *m*/*z* 340.25, 246.23, 218.20, and 102.12, indicating the formation of intermediate compounds.[75,76] These fragments result from processes such as demethylation, decarbonylation, and ring-opening of the CV molecule. With continued oxidation up to 90 min, the degradation proceeds to full mineralization, ultimately producing carbon dioxide and water as the final products.

To investigate the potential degradation pathways of CR, LC-MS analysis was conducted by collecting samples of both intermediate and final stable degradation products, as illustrated in Fig. S11.† The proposed chemical structures of the main decomposition products of CR treatment with $SrTiO_3$/PHI under irradiation for 90 min are presented. The LC-MS spectrum of the CR solution at intermediate stages of the degradation process shows fragmentation peaks at 371.03, 176.12, 158.08 and 97.07 *m*/*z*.[77,78] The various mass

fragments observed in the CR dye solution likely result from the cleavage of specific chemical bonds during the degradation process by cleavage of the benzene ring and sulfonate group and cleavage of various C–N and C–C bonds of the chromophore group.[79] During irradiation, the dye solution generates a high concentration of reactive hydroxyl radicals ($^{\bullet}OH$), which tend to attack molecular sites with high electron density. The mass spectrum further confirms this activity by displaying ion peaks such as HSO_4^- at m/z 97.07.[80] The mass spectrum clearly indicates that the high-mass fragments of CR have been eliminated.

3.12. Possible photocatalytic mechanism

The improved photocatalytic activity of the $SrTiO_3$ NCs/PHI heterostructure was further studied by examining charge transfer and the reaction pathways of photogenerated electrons and holes. The roles of $O_2^{\bullet-}$, h^+, e^-, and $OH^{\bullet}$ radicals in photocatalytic degradation of CV and CR were examined using *p*-BQ, DMSO, sodium citrate, and IPA as scavengers, respectively. The photodegradation of CV is primarily mediated by $O_2^{\bullet-}$ and e^-, which are followed in importance by holes and $OH^{\bullet}$ radicals, respectively. Hydroxyl radicals are the main players in photodegradation of CV.[81] The presence of *p*-BQ/$O_2^{\bullet-}$ significantly decreased the photodegradation, which was then followed by sodium citrate/e^-, and IPA/$OH^{\bullet}$. This indicates that the $O_2^{\bullet-}$ radical is the major radical in CR photodegradation.[82] The degradation efficiency and kinetic rate constant of scavenging tests of CV and CR are described in Fig. 6d and 7d.

To evaluate the generation of superoxide radicals ($^{\bullet}O_2^-$) in the $SrTiO_3$ NCs/PHI heterojunction system under visible light, nitro blue tetrazolium chloride (NBT) was employed as a selective molecular probe. The characteristic absorbance of NBT at 260 nm was monitored using UV-vis spectroscopy (Fig. S12a†). Upon UV irradiation, a progressive decrease in the absorbance at 260 nm was observed, indicating the consumption of NBT due to its reaction with photogenerated $^{\bullet}O_2^-$ radicals. This decline in NBT absorbance confirms its reduction to formazan, which does not absorb significantly at 260 nm. The observed trend supports the formation of $^{\bullet}O_2^-$ *via* electron transfer from the conduction band of PHI (−0.53 eV), where photoexcited electrons, originating from $SrTiO_3$ (−0.63 eV), accumulate due to type I band alignment. The efficient separation and migration of charge carriers under UV illumination enhance the reduction of dissolved oxygen to superoxide radicals, which subsequently react with NBT. The results provide strong evidence of active $^{\bullet}O_2^-$ generation in the $SrTiO_3$ NCs/PHI system, validating its photocatalytic potential and the role of NBT as an effective probe for superoxide detection.[83]

The generation of hydroxyl radicals ($^{\bullet}OH$) by the $SrTiO_3$ NCs/PHI heterojunction was investigated using terephthalic acid (TA) as a photoluminescence (PL) probe. TA reacts specifically with $^{\bullet}OH$ to form 2-hydroxyterephthalic acid, which emits a characteristic fluorescence peak at 410 nm (Fig. S12b†). Under visible light irradiation, a steady increase in PL intensity at 410 nm was observed over time, confirming the formation of $^{\bullet}OH$ radicals. However, when comparing the composite ($SrTiO_3$ NCs/PHI) with the individual components, a significantly lower PL intensity was recorded for the composite system. This indicates reduced $^{\bullet}OH$ generation in the heterojunction, which can be explained by the type I charge transfer pathway. In this mechanism, photogenerated electrons in PHI (E_{CB} = −0.53 eV) transfer to the conduction band of $SrTiO_3$ NCs (E_{CB} = −0.63 eV), promoting the reduction of O_2 to superoxide ($^{\bullet}O_2^-$) rather than generating $^{\bullet}OH$ through water oxidation. Furthermore, the valence band of PHI (2.20 eV) is not positive enough to oxidize water to $^{\bullet}OH$ (oxidation potential ~2.38 eV), while $SrTiO_3$ NCs (E_{VB} = 2.63 eV) can, but hole transfer from PHI to $SrTiO_3$ NCs is limited due to unfavourable band alignment. These results confirm that in the $SrTiO_3$ NCs/PHI system, the type I mechanism promotes superoxide radical formation over hydroxyl radical generation, consistent with the observed decrease in PL intensity at 410 nm.[84]

Based on the above scavenger results, a possible mechanism for the $SrTiO_3$ NCs/PHI photocatalyst with improved activity is proposed, as shown in Fig. 8g. The conduction/valence band positions, bandgap, and light-harvesting ability can be evaluated *via* Mott–Schottky plots, the Kubelka–Munk method, and UV-vis DRS. Fig. 4a shows $SrTiO_3$ NCs with an absorption edge at ~380 nm (bandgap: 3.25 eV, Fig. 4b). PHI modification redshifts the edge to 450–500 nm, boosting visible-light absorption and photocarrier generation. $SrTiO_3$ NCs/PHI itself absorbs broadly (200–800 nm) with a 2.53 eV bandgap (Fig. 4d). From the Mott–Schottky curves (Fig. 8(e and f)), the E_{fb} values for $SrTiO_3$ NCs and PHI are −0.63 V and −0.53 V *vs.* SCE. Using $E_g = E_{VB} - E_{CB}$, $SrTiO_3$ NCs and PHI show E_{VB} of 2.63 eV and 2.20 eV, with corresponding E_{CB} of −0.63 eV and −0.53 eV.

The h^+ oxidation potentials for $OH^{\bullet}/OH^-$ and $OH^{\bullet}/H_2O$ are reported to be +1.99 eV and +2.7 eV *vs.* NHE, respectively. The E_{VB} values of $SrTiO_3$ NCs (+2.63 eV) and PHI (+2.20 eV) *vs.* NHE exceed the redox potentials of $OH^{\bullet}/OH^-$ and $OH^{\bullet}/H_2O$, indicating that their photoholes can oxidize OH^- and H_2O to $OH^{\bullet}$ thermodynamically. $SrTiO_3$ NCs and PHI are n-type semiconductors with Fermi levels near their conduction bands. An n–n heterojunction is successfully formed at their interface. Under light irradiation, electrons in $SrTiO_3$ NCs and PHI are excited to the CB, leaving holes in the VB. Since the CB potential of $SrTiO_3$ NCs is lower than that of PHI, electrons in $SrTiO_3$ NCs migrate to PHI until Fermi level equilibrium is reached. Even then, the built-in electric field at the $SrTiO_3$ NCs/PHI n–n heterojunction interface continues to drive electron transfer. Such an electron transfer path restrains photoexcited electrons–holes from recombining and further enhances the photocatalytic activity. Simultaneously, the CB electrons of $SrTiO_3$ NCs capture O_2 molecules and reduce them to $O_2^{\bullet-}$ owing to its lower potential (−0.365 V *vs.* NHE) in aqueous solution at pH 0 than that of $O_2/O_2^{\bullet-}$ (−0.33 V *vs.* NHE), while VB holes of $SrTiO_3$ NCs and PHI oxidize H_2O or OH^- to form $OH^{\bullet}$. Afterward, $O_2^{\bullet-}$ and $OH^{\bullet}$ directly

decompose pollutants (CV, MB, RhB and CR) to CO_2, H_2O, and other small molecules.

The whole reaction process is summed up as follows:

$$SrTiO_3NCs + h\upsilon \rightarrow SrTiO_3NCs + h^+ + e^- \quad (1)$$

$$PHI + h\upsilon \rightarrow PHI + h^+ + e^- \quad (2)$$

$$O_2 + e^- \rightarrow O_2^{\bullet -} \quad (3)$$

$$h^+ + H_2O \rightarrow OH^\bullet + H^+ \quad (4)$$

$$h^+ + OH^- \rightarrow OH^\bullet \quad (5)$$

$$O_2^{\bullet -} + OH^\bullet + \text{Pollutant(CV, MB, RhB and CR)} \rightarrow CO_2 + H_2O + \text{small molecules} \quad (6)$$

4. Conclusion

In summary, an effective heterojunction photocatalyst, $SrTiO_3$ NCs/PHI, driven by visible light has been successfully designed for the photocatalytic degradation of multiple dyes. The morphology, structure, chemical composition, and surface functional groups of the composite were thoroughly characterized using standard techniques. The study revealed that the $SrTiO_3$ NCs/PHI composite exhibits a significantly higher degradation rate compared to bare $SrTiO_3$ NCs and PHI. The proposed $SrTiO_3$ NCs/PHI catalyst demonstrated excellent rate constants of 0.0165, 0.0245, 0.0158, and 0.0228 min^{-1} for CR, CV, RhB, and MB, respectively. Additionally, $SrTiO_3$ NCs/PHI efficiently degraded azo dyes within 90 minutes (CR, CV, and MB) and RhB within 150 min. The enhanced performance of the $SrTiO_3$ NCs/PHI hybrid composite can be attributed to the extended visible light absorption provided by PHI and the formation of a heterojunction, which suppresses photogenerated charge recombination and increases charge carrier lifetimes. Furthermore, a plausible mechanism for the photodegradation of azo dyes was proposed, highlighting the promising potential of the $SrTiO_3$ NCs/PHI photocatalyst in industrial wastewater treatment. In summary, the $SrTiO_3$ NCs/PHI composite demonstrated effective photocatalytic degradation of organic pollutants under visible light. In future work, efforts will be directed toward optimizing the interfacial contact, enhancing solar-light-driven activity, and evaluating the system under real wastewater conditions. Further studies will also investigate the long-term stability of the catalyst, metal ion leaching, and by-product toxicity to ensure environmental safety and practical viability.

Data availability

The data that support the findings of this study are available from the corresponding author upon reasonable request.

Author contributions

Phyu Phyu Cho: writing – original draft, visualization, methodology, investigation, formal analysis, data curation, conceptualization, writing – review & editing. Phyu Phyu Mon: methodology, formal analysis, investigation. Mohit Kumar: investigation, methodology, software. Suryakala Duvvuri: validation, formal analysis. Giridhar Madras: writing – review & editing. Guo-Ping Chang-Chien: software, writing – review & editing. Srinivaas Masimukku: software, writing – review & editing. Challapalli Subrahmanyam: conceptualization, writing – review & editing, visualization, validation, supervision, project administration, funding acquisition.

Conflicts of interest

There are no conflicts to declare.

Acknowledgements

Phyu Phyu Cho and Phyu Phyu Mon are thankful to DIA-Doctoral Fellowship in India for ASEAN for financial assistance and the Indian Institute of Technology Hyderabad for facility support. Mohit Kumar would like to thank the CSIR-India for a senior research fellowship and Swinburne University of Technology, Australia for a SUPRA fellowship.

References

1 R. Gade, J. Ahemed, K. L. Yanapu, S. Y. Abate, Y.-T. Tao and S. Pola, *J. Environ. Chem. Eng.*, 2018, **6**, 4504–4513.
2 V. D. Rao, M. Subburu, R. Gade, M. Basude, P. Chetti, N. B. Simhachalam, P. Nagababu, Y. Bhongiri and S. Pola, *Environ. Sci.: Water Res. Technol.*, 2021, **7**, 1737.
3 R. Parikirala, R. Kore, V. Rohini, D. Venkateshwar Rao, P. Chetti and S. Pola, *J. Environ. Chem. Eng.*, 2024, **12**, 113471.
4 R. Vallavoju, R. Kore, P. Radhika, M. Subburu, R. Gade, M. Basude, S. Pola and P. Chetti, *Inorg. Chem. Commun.*, 2023, **148**, 110272.
5 R. Vallavoju, R. Kore, R. P., M. Subburu, M. Basude, P. Chetti and S. Pola, *J. Photochem. Photobiol., A*, 2023, **442**, 114775.
6 M. Subburu, R. Gade, V. Guguloth, P. Chetti, K. R. Ravulapelly and S. Pola, *J. Photochem. Photobiol., A*, 2021, **406**, 112996.
7 J. Ahemed, J. Pasha, D. V. Rao, R. Kore, R. Gade, Y. Bhongiri, P. Chetti and S. Pola, *J. Photochem. Photobiol., A*, 2021, **419**, 113455.
8 V. Guguloth, J. Ahemed, M. Subburu, V. C. Guguloth, P. Chetti and S. Pola, *J. Photochem. Photobiol., A*, 2019, **382**, 111975.
9 K. Masula, P. Sreedhar, P. V. Kumar, Y. Bhongiri, S. Pola and M. Basude, *Mater. Sci. Semicond. Process.*, 2023, **160**, 107432.
10 K. Masula, Y. Bhongiri, G. R. Rao, P. V. Kumar, S. Pola and M. Basude, *Opt. Mater.*, 2022, **126**, 112201.
11 A. B. Siddique, M. A. Shaheen, A. Abbas, Y. Zaman, M. A. Bratty, A. Najmi, A. Hanbashi, M. Mustaqeem, H. A. Alhazmi, Z. ur Rehman, K. Zoghebi and H. M. A. Amin, *Heliyon*, 2024, **10**(23), e40679.

12 A. B. Siddique, D. Amr, A. Abbas, L. Zohra, M. I. Irfan, A. Alhoshani, S. Ashraf and H. M. A. Amin, *Int. J. Biol. Macromol.*, 2024, **256**, 128009.
13 A. Ejaz, Z. Mamtaz, I. Yasmin, M. Shaban, A. B. Siddique, M. I. Irfan, A. Ali, S. Muhammad, M. Y. Sameeh and A. Abbas, *J. Mol. Liq.*, 2024, **393**, 123622.
14 N. Assad, A. Abbas, M. F. ur Rehman and M. Naeem-ul-Hassan, *RSC Adv.*, 2024, **14**, 22344–22358.
15 L. Shen, X. Chen, Y. Chen, J. Peng, A. Abbas, J. Wei, C. Yu, J. Li and Y. Li, *J. Electron. Mater.*, 2022, **51**, 3092–3100.
16 S. Ghaffar, A. Abbas, M. Naeem-ul-Hassan, N. Assad, M. Sher, S. Ullah, H. A. Alhazmi, A. Najmi, K. Zoghebi, M. Al Bratty, A. Hanbashi, H. A. Makeen and H. M. A. Amin, *Antioxidants*, 2023, **12**, 1201.
17 R. Gade, M. Basude, N. B. Simhachalam, V. D. Rao, S. Pola and P. Chetti, *Environ. Sci.: Water Res. Technol.*, 2022, **8**, 3065–3078.
18 A. W. Khan, N. S. Lali, F. Y. Sabei, M. I. Irfan, M. Naeem-ul-Hassan, M. Sher, A. Y. Safhi, A. Alsalhi, A. H. Albariqi, F. Kamli, H. M. A. Amin and A. Abbas, *J. Environ. Chem. Eng.*, 2024, **12**, 112576.
19 L. D. Namade, S. S. Band, P. K. Pawar, A. R. Patil, R. S. Pedanekar, K. G. Managave, V. V. Ganbavle and K. Y. Rajpure, *Colloids Surf., A*, 2025, **708**, 135976.
20 M. Rezaei, A. A. Ensafi and E. Heydari-Bafrooei, *Colloids Surf., A*, 2025, **708**, 135993.
21 M. Ahmadi, M. S. Seyed Dorraji, M. H. Rasoulifard and A. R. Amani-Ghadim, *Sep. Purif. Technol.*, 2019, **228**, 115771.
22 M. Ganesan, I. P. Chinnuraj, R. Rajendran, T. Rojviroon, O. Rojviroon, P. Thangavelu and S. Sirivithayapakorn, *Diamond Relat. Mater.*, 2025, **155**, 112254.
23 M. Awan, S. Rauf, A. Abbas, M. H. Nawaz, C. Yang, S. A. Shahid, N. Amin and A. Hayat, *J. Mol. Liq.*, 2020, **317**, 114014.
24 A. Abbas, H. M. A. Amin, M. Akhtar, M. A. Hussain, C. Batchelor-McAuley and R. G. Compton, *Chem. Naissensis*, 2020, **3**(1), 50–70.
25 J. Tang, L. Shen, K. Zhao, J. Peng, Q. Chen, C. Yu, Y. Li, A. Abbas, S. Wang and Z. Liu, *Appl. Surf. Sci.*, 2024, **643**, 158574.
26 H. Zhang, Z. Xia, P. Niu, X. Zhi, R. Dai, S. Chen, S. Wang and L. Li, *Catal. Sci. Technol.*, 2022, **12**, 5372–5378.
27 L. Lin, Z. Yu and X. Wang, *Am. Ethnol.*, 2019, **131**, 6225–6236.
28 B. V. Lotsch, M. Döblinger, J. Sehnert, L. Seyfarth, J. Senker, O. Oeckler and W. Schnick, *Chem. – Eur. J.*, 2007, **13**, 4969–4980.
29 M. Liu, C. Wei, H. Zhuzhang, J. Zhou, Z. Pan, W. Lin, Z. Yu, G. Zhang and X. Wang, *Angew. Chem., Int. Ed.*, 2022, **61**, e202113389.
30 Z. Chen, A. Savateev, S. Pronkin, V. Papaefthimiou, C. Wolff, M. G. Willinger, E. Willinger, D. Neher, M. Antonietti and D. Dontsova, *Adv. Mater.*, 2017, **29**, 1700555.
31 F. M. Colombari, M. A. R. da Silva, M. S. Homsi, B. R. L. de Souza, M. Araujo, J. L. Francisco, G. T. S. T. da Silva, I. F. Silva, A. F. de Moura and I. F. Teixeira, *Faraday Discuss.*, 2021, **227**, 306–320.
32 N. A. Rodríguez, A. Savateev, M. A. Grela and D. Dontsova, *ACS Appl. Mater. Interfaces*, 2017, **9**, 22941–22949.
33 D. Gong, J. G. Highfield, S. Z. E. Ng, Y. Tang, W. C. J. Ho, Q. Tay and Z. Chen, *ACS Sustainable Chem. Eng.*, 2014, **2**, 149–157.
34 M. A. Elkodous, A. M. El-Khawaga, M. M. Abouelela and M. I. A. A. Maksoud, *Sci. Rep.*, 2023, **13**, 6331.
35 H. Zhang, Z. Xia, P. Niu, X. Zhi, R. Dai, S. Chen, S. Wang and L. Li, *Catal. Sci. Technol.*, 2022, **12**, 5372–5378.
36 T. Sureshkumar, S. Thiripuranthagan, S. M. K. Paskalis, S. Kumaravel, K. Kannan and A. Devarajan, *J. Photochem. Photobiol., A*, 2018, **356**, 425–439.
37 G. Liu, M. Liao, Z. Zhang, H. Wang, D. Chen and Y. Feng, *Sep. Purif. Technol.*, 2020, **244**, 116618.
38 M. Sohrabian, V. Mahdikhah, E. Alimohammadi and S. Sheibani, *Appl. Surf. Sci.*, 2023, **618**, 156682.
39 J. Kröger, A. Jiménez-Solano, G. Savasci, P. Rovó, I. Moudrakovski, K. Küster, H. Schlomberg, H. A. Vignolo-González, V. Duppel, L. Grunenberg, C. B. Dayan, M. Sitti, F. Podjaski, C. Ochsenfeld and B. V. Lotsch, *Adv. Energy Mater.*, 2021, **11**, 2003016.
40 M. Akilarasan, E. Tamilalagan, S.-M. Chen, S. Maheshwaran, T.-W. Chen, A. M. Al-Mohaimeed, W. A. Al-Onazi and M. S. Elshikh, *Microchim. Acta*, 2021, **188**, 72.
41 D. Yu-Lei, C. Guang, Z. Ming-Sheng and Y. Sen-Zu, *Chin. Phys. Lett.*, 2003, **20**, 1561.
42 Q. I. Rahman, S. Hasan, A. Ali, S. K. Mehta, M. A. Raja, N. Ahmad, A. R. Khan and M. Muddassir, *J. Nanosci. Nanotechnol.*, 2020, **20**, 6475–6481.
43 S. Kogularasu, M. Govindasamy, S.-M. Chen, M. Akilarasan and V. Mani, *Sens. Actuators, B*, 2017, **253**, 773–783.
44 L. Dong, Q. Luo, K. Cheng, H. Shi, Q. Wang, W. Weng and W.-Q. Han, *Sci. Rep.*, 2014, **4**, 5084.
45 F. A. Rabuffetti, H.-S. Kim, J. A. Enterkin, Y. Wang, C. H. Lanier, L. D. Marks, K. R. Poeppelmeier and P. C. Stair, *Chem. Mater.*, 2008, **20**, 5628–5635.
46 Y. Jiang, X. Tang, Y. Zhou and Q. Liu, *Prog. Nat. Sci.: Mater. Int.*, 2011, **21**, 198–204.
47 F. Puleo, L. F. Liotta, V. La Parola, D. Banerjee, A. Martorana and A. Longo, *Phys. Chem. Chem. Phys.*, 2014, **16**, 22677–22686.
48 J. Jia, D. Li, J. Wan and X. Yu, *J. Ind. Eng. Chem.*, 2016, **33**, 162–169.
49 S. Le, T. Jiang, Y. Li, Q. Zhao, Y. Li, W. Fang and M. Gong, *Appl. Catal., A*, 2017, **200**, 601–610.
50 S. Kumar, S. Tonda, A. Baruah, B. Kumar and V. Shanker, *Dalton Trans.*, 2014, **43**, 16105–16114.
51 A. R. Benrekia, N. Benkhettou, A. Nassour, M. Driz, M. Sahnoun and S. Lebègue, *Phys. B*, 2012, **407**, 2632–2636.
52 E. Zhou, J.-M. Raulot, H. Xu, H. Hao, Z. Shen and H. Liu, *Phys. B*, 2022, **643**, 414160.
53 Y. Duan, P. Ohodnicki, B. Chorpening and G. Hackett, *J. Solid State Chem.*, 2017, **256**, 239–251.
54 T. Jia, Z. Zeng, H. Q. Lin, Y. Duan and P. Ohodnicki, *RSC Adv.*, 2017, **7**, 38798–38804.
55 H. Bentour, M. El Yadari, A. El Kenz and A. Benyoussef, *Solid State Commun.*, 2020, **312**, 113893.

56 U. S. Shenoy, H. Bantawal and D. K. Bhat, *J. Phys. Chem. C*, 2018, **122**, 27567–27574.
57 H. Schlomberg, J. Kröger, G. Savasci, M. W. Terban, S. Bette, I. Moudrakovski, V. Duppel, F. Podjaski, R. Siegel, J. Senker, R. E. Dinnebier, C. Ochsenfeld and B. V. Lotsch, *Chem. Mater.*, 2019, **31**, 7478–7486.
58 M. Döblinger, B. V. Lotsch, J. Wack, J. Thun, J. Senker and W. Schnick, *Chem. Commun.*, 2009, 1541–1543.
59 V. W. Lau, I. Moudrakovski, T. Botari, S. Weinberger, M. B. Mesch, V. Duppel, J. Senker, V. Blum and B. V. Lotsch, *Nat. Commun.*, 2016, **7**, 12165.
60 T. Tyborski, C. Merschjann, S. Orthmann, F. Yang, M.-C. Lux-Steiner and T. Schedel-Niedrig, *J. Phys.: Condens. Matter*, 2012, **24**, 162201.
61 B. Jürgens, E. Irran, J. Senker, P. Kroll, H. Müller and W. Schnick, *J. Am. Chem. Soc.*, 2003, **125**, 10288–10300.
62 S. Sharafinia, A. Farrokhnia, E. G. Lemraski and A. Rashidi, *Sci. Rep.*, 2023, **13**, 21323.
63 K. Sharifian, V. Mahdikhah and S. Sheibani, *Ceram. Int.*, 2021, **47**, 22741–22752.
64 M. A. Ferreira, G. T. S. T. da Silva, O. F. Lopes, V. R. Mastelaro, C. Ribeiro, M. J. M. Pires, A. R. Malagutti, W. Avansi and H. A. J. L. Mourão, *Mater. Sci. Semicond. Process.*, 2020, **108**, 104887.
65 P. P. Cho, P. P. Mon, K. V. A. Kumar, M. Kumar, P. Ghosal, N. Lingaiah, G. Madras and C. Subrahmanyam, *Inorg. Chem. Commun.*, 2023, **156**, 111147.
66 M. Ahmad, M. T. Qureshi, W. Rehman, N. H. Alotaibi, A. Gul, R. S. A. Hameed, M. A. Elaimi, M. F. H. A. El-kader, M. Nawaz and R. Ullah, *J. Alloys Compd.*, 2022, **895**, 162636.
67 N. Arabpour and A. Nezamzadeh-Ejhieh, *Mater. Sci. Semicond. Process.*, 2015, **31**, 684–692.
68 Y.-K. Chang, J.-E. Chang and L.-C. Chiang, *Chemosphere*, 2003, **52**, 1089–1094.
69 C. Chen, Q. Zuo, D. Wu, X. Yao and Y. Tian, *Appl. Surf. Sci.*, 2025, **690**, 162597.
70 S. J. Petrović, G. D. Bogdanović and M. M. Antonijević, *Trans. Nonferrous Met. Soc. China*, 2018, **28**, 1444–1455.
71 T. Havlik, D. Orac, M. Petranikova, A. Miskufova, F. Kukurugya and Z. Takacova, *J. Hazard. Mater.*, 2010, **183**, 866–873.
72 Y.-R. Huang, Y. Kong, H.-Z. Li and X.-M. Wei, *Environ. Technol. Innovation*, 2020, **18**, 100780.
73 S. Ramanathan, R. M. Rashmitha, H.-C. Chuang, J. Kasemchainan, M. K. Arumugam, I. S. Lydia, S. Pandiyarajan and S. Poompradub, *Process Saf. Environ. Prot.*, 2024, **187**, 145–158.
74 S. Mallakpour and V. Ramezanzade, *J. Environ. Manage.*, 2021, **291**, 112680.
75 X. Liu and J. Wang, *Environ. Pollut.*, 2024, **350**, 124037.
76 M. F. Sanakousar, C. Vidyasagar, V. M. Jiménez-Pérez, B. K. Jayanna, Mounesh, A. H. Shridhar and K. Prakash, *J. Hazard. Mater. Adv.*, 2021, **2**, 100004.
77 V. Gadore, A. K. Singh, S. R. Mishra and M. Ahmaruzzaman, *Sci. Rep.*, 2024, **14**, 1118.
78 R. R. M. Khan, H. Qamar, A. Hameed, A. ur Rehman, M. Pervaiz, Z. Saeed, A. Adnan and A. R. Ch, *Water, Air, Soil Pollut.*, 2022, **233**, 468.
79 M. Maruthapandi, A. Saravanan, P. Manohar, J. H. T. Luong and A. Gedanken, *Nanomaterials*, 2021, **11**, 1128.
80 N. F. Zainudin, S. T. Sam, Y. S. Wong, H. Ismail, S. Walli, K. Inoue, G. Kawamura and W. K. Tan, *Polymers*, 2023, **15**, 237.
81 X. Zheng, J. Yuan, S. Jing, J. Liang, J. Che, B. Tang, G. He and H. Chen, *J. Mater. Sci.: Mater. Electron.*, 2019, **30**, 5986–5994.
82 K. Javed, N. Abbas, M. Bilal, A. A. Alshihri, H. Z. Rab Nawaz, M. F. Ramadan and S. A. R. Naqvi, *RSC Adv.*, 2024, **14**, 30957.
83 N. K. Tailor, M. Abdi-Jalebi, V. Gupta, H. Hu, M. I. Dar, G. Li and S. Satapathi, *J. Mater. Chem. A*, 2020, **8**, 21356–21386.
84 F. Cheng and J. Wang, *ACS ES&T Water*, 2024, **4**, 5077–5088.